



# Mixed Noble-Gas Compounds of Krypton(II) and Xenon(VI); $[F_5Xe(FKrF)AsF_6]$ and $[F_5Xe(FKrF)_2AsF_6]$

Matic Lozinšek,\* H el ene P. A. Mercier,\* and Gary J. Schrobilgen\*

Dedicated to Professor Boris  zemva on the occasion of his 80th birthday

**Abstract:** The coordination chemistry of  $KrF_2$  has been limited in contrast with that of  $XeF_2$ , which exhibits a far richer coordination chemistry with main-group and transition-metal cations. In the present work, reactions of  $[XeF_5][AsF_6]$  with  $KrF_2$  in anhydrous HF solvent afforded  $[F_5Xe(FKrF)AsF_6]$  and  $[F_5Xe(FKrF)_2AsF_6]$ , the first mixed krypton/xenon compounds. X-ray crystal structures and Raman spectra show the  $KrF_2$  ligands and  $[AsF_6]^-$  anions are F-coordinated to the xenon atoms of the  $[XeF_5]^+$  cations. Quantum-chemical calculations are consistent with essentially noncovalent ligand–xenon bonds that may be described in terms of  $\sigma$ -hole bonding. These complexes significantly extend the  $XeF_2$ – $KrF_2$  analogy and the limited chemistry of krypton by introducing a new class of coordination compound in which  $KrF_2$  functions as a ligand that coordinates to xenon(VI). The HF solvates,  $[F_5Xe(FH)AsF_6]$  and  $[F_5Xe(FH)SbF_6]$ , are also characterized in this study and they provide rare examples of HF coordinated to xenon(VI).

## Introduction

Krypton reactivity was discovered<sup>[1]</sup> soon after the landmark synthesis of the first true noble-gas compound,  $Xe[PtF_6]$ .<sup>[2]</sup> Although the precise formulation of  $Xe[PtF_6]$  remains unproven, it is likely a salt or a mixture of  $[XeF]^+$  salts.<sup>[3,4]</sup> Although the discoveries of xenon and krypton chemical reactivities occurred nearly 60 years ago and within a year of one another, their chemistries never became entwined to form a single compound that contains both chemically bound noble gases. In contrast with xenon, which

exhibits formal oxidation states in its isolated compounds of 0,  $+1/2$ , +2, +4, +6, and +8, krypton only exhibits the +2 oxidation state and a far more limited chemistry. The only binary krypton fluoride that can be synthesized in macroscopic and synthetically useful amounts is  $KrF_2$ ,<sup>[5–7]</sup> from which all other krypton compounds have been derived.<sup>[5–12]</sup>

Prior studies have explored the ligating properties of  $KrF_2$  and have provided several  $KrF_2$  adducts that were structurally characterized by low-temperature (LT) single-crystal X-ray diffraction (SCXRD) and Raman spectroscopy. The latter include complexes with a main-group  $Br^V$  oxyfluoride cation,  $[F_2OBr(FKrF)_2AsF_6]$ ,<sup>[8]</sup> a neutral covalent transition-metal  $Hg^{II}$  compound,  $Hg(OTeF_5)_2 \cdot 1.5KrF_2$ ,<sup>[9]</sup> a transition-metal cation,  $Hg^{2+}$ ,  $[Hg(FKrF)_8][AsF_6]_2$ ,<sup>[11]</sup> and a main-group metal cation,  $Mg^{2+}$ ,  $[Mg(FKrF)_4(AsF_6)_2]$ .<sup>[10]</sup> Most recently, the  $KrF_2$  adducts of the weak fluoride-ion acceptor,  $CrOF_4$ , have been reported and structurally characterized for  $KrF_2 \cdot nCrOF_4$  ( $n = 1, 2$ ).<sup>[12]</sup> The xenon analogues,  $[F_2OBr(FXeF)_2AsF_6]$ ,<sup>[13]</sup>  $Hg(OTeF_5)_2 \cdot 1.5XeF_2$ ,<sup>[9]</sup>  $XeF_2 \cdot nCrOF_4$  ( $n = 1, 2$ ),<sup>[12]</sup> and  $[Mg(FXeF)_4(AsF_6)_2]$ <sup>[14]</sup> have also been synthesized and structurally characterized by SCXRD and Raman spectroscopy. The linear, centrosymmetric ( $D_{\infty h}$ )  $NgF_2$  ( $Ng = Kr, Xe$ ) molecules<sup>[15]</sup> distort upon coordination to a fluoride-ion acceptor (A) to form a  $Ng-F_b \cdots A$  bridge in which the  $Ng-F_b$  bond is elongated and the terminal  $Ng-F_t$  bond is contracted relative to free  $NgF_2$ . The extent to which distortion and polarization of the  $NgF_2$  ligand occurs, and thus the extent to which the positive charge on Ng is enhanced, depends on the Lewis acidity of the fluoride-ion acceptor.<sup>[5,6,16]</sup> Interactions with the strongly Lewis acidic pnictogen pentafluorides,  $PnF_5$ , result in the formation of strongly ion-paired  $[NgF][PnF_6]$ <sup>[6,15]</sup> salts in which the  $[NgF]^+$  cations and  $[PnF_6]^-$  anions interact by means of  $Ng \cdots F_b-Pn$  bridges. The electrophilicities of  $[NgF]^+$  and coordinated  $NgF_2$  ligands relative to free  $NgF_2$  are manifested by marked increases in their oxidative fluorinating abilities.<sup>[5]</sup> In the case of  $KrF_2$ , the number of suitable Lewis acids that can coordinate to  $KrF_2$  and withstand its extraordinary oxidative fluorinating strength is very limited.

Two criteria must therefore be met for the formation of a mixed xenon/krypton adduct: (1) The fluorobasicity of  $KrF_2$  must closely balance the Lewis acidity of the xenon substrate, i.e., a Lewis acid that is too weak will be unable to coordinate  $KrF_2$ , whereas a Lewis acid that is too strong will abstract  $F^-$  to form a more electrophilic and strongly oxidizing  $[KrF]^+$  salt. (2) The fluoride-ion acceptor must be sufficiently resistant to attack by the potent oxidative fluorinator,  $KrF_2$ . The Lewis acidic  $[XeF_5]^+$  cation meets these criteria by virtue of its net positive charge and the high formal oxidation state of xenon (+6).

[\*] Dr. M. Lozinšek, Dr. H. P. A. Mercier, Prof. Dr. G. J. Schrobilgen  
Department of Chemistry, McMaster University  
Hamilton, ON L8S 4M1 (Canada)  
E-mail: mercierhpa@live.com  
schrobil@mcmaster.ca

Dr. M. Lozinšek  
Present address: Department of Inorganic Chemistry and Technology, Jo ef Stefan Institute  
Jamova 39, 1000 Ljubljana (Slovenia)  
E-mail: matic.lozinsek@ijs.si

Supporting information and the ORCID identification number(s) for the author(s) of this article can be found under:  
<https://doi.org/10.1002/anie.202014682>.

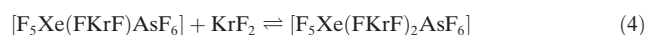
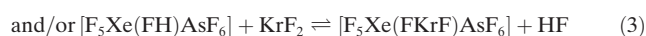
  2020 The Authors. Angewandte Chemie International Edition published by Wiley-VCH GmbH. This is an open access article under the terms of the Creative Commons Attribution Non-Commercial NoDerivs License, which permits use and distribution in any medium, provided the original work is properly cited, the use is non-commercial and no modifications or adaptations are made.

The coordination behavior of the  $[\text{XeF}_5]^+$  cation in its salts is well documented for Xe--F<sub>b</sub> interactions between the  $[\text{XeF}_5]^+$  cations and their counteranions.<sup>[17]</sup> Examples in which  $[\text{XeF}_5]^+$  is coordinated to a XeF<sub>2</sub> ligand are known, for  $[\text{F}_5\text{Xe}(\text{FXeF})\text{XeF}_5(\text{AsF}_6)_2]$ ,  $[\text{F}_5\text{Xe}(\text{FXeF})\text{AsF}_6]$ , and  $[\text{F}_5\text{Xe}(\text{FXeF})_2\text{AsF}_6]$ ,<sup>[18,19]</sup> which were characterized by SCXRD and Raman spectroscopy, and  $[\text{F}_5\text{Xe}(\text{FXeF})\text{RuF}_6]$ ,<sup>[20]</sup> which was characterized by Raman spectroscopy. In contrast, the cocrystal,  $[\text{XeF}_5][\text{SbF}_6]\cdot\text{XeOF}_4$ ,<sup>[21]</sup> exhibits no interactions between  $[\text{XeF}_5]^+$  and  $\text{XeOF}_4$ , in accordance with the low relative fluorobasicity of  $\text{XeOF}_4$ .

## Results and Discussion

### Syntheses

In the present work, the Lewis acidity of the  $[\text{XeF}_5]^+$  cation and the fluorobasic character of  $\text{KrF}_2$  have been exploited for the syntheses of the first mixed noble-gas (Kr/Xe) compounds that are isolable in macroscopic quantities. The products obtained from the LT reactions of  $[\text{XeF}_5][\text{AsF}_6]$  and  $\text{KrF}_2$  in anhydrous HF (aHF) solvent and subsequent crystallizations at LT depended on the initial  $\text{KrF}_2$ : $[\text{XeF}_5]$ - $[\text{AsF}_6]$  molar ratio. The complex,  $[\text{F}_5\text{Xe}(\text{FKrF})\text{AsF}_6]$  (**1**), was obtained by use of a 1.5:1 molar ratio of reactants, whereas a stoichiometric excess of  $\text{KrF}_2$  (3.5:1 or 2.1:1) resulted in  $[\text{F}_5\text{Xe}(\text{FKrF})_2\text{AsF}_6]$  (**2**). In an attempt to prepare the  $\text{KrF}_2$  analogue of  $[\text{F}_5\text{Xe}(\text{FXeF})\text{XeF}_5(\text{AsF}_6)_2]$ ,<sup>[19]</sup> a 1:1.9 molar ratio of reactants was used, which resulted in crystallization of **1** and  $[\text{F}_5\text{Xe}(\text{FH})\text{AsF}_6]$  (**3**). Compound **3** was also isolated from an aHF solution of  $[\text{XeF}_5][\text{AsF}_6]$  upon removal of HF at LT. The synthesis of the antimony analogue  $[\text{F}_5\text{Xe}(\text{FH})\text{SbF}_6]$  (**4**) is described in the Supporting Information. The syntheses of **1–3** are in accordance with the proposed Equilibria (1)–(4), which are supported by LT SCXRD structure determinations of the adduct-cation salts,  $[\text{F}_5\text{Xe}(\text{FKrF})\text{AsF}_6]$  and  $[\text{F}_5\text{Xe}(\text{FKrF})_2\text{AsF}_6]$ , and the intermediate solvate,  $[\text{F}_5\text{Xe}(\text{FH})\text{AsF}_6]$ , as well as by LT Raman spectroscopy. Vibrational frequency assignments were aided by calculated frequencies and intensities obtained from DFT calculations (vide infra). It is apparent that HF also behaves as a weak ligand towards  $[\text{XeF}_5]^+$  in an HF solution and that  $\text{KrF}_2$ , a somewhat less fluorobasic ligand than  $\text{XeF}_2$ ,<sup>[22]</sup> is sufficiently fluorobasic to displace HF to form  $[\text{F}_5\text{Xe}(\text{FKrF})\text{AsF}_6]$  [Eq. (3)].



### X-ray Crystallography

Details of X-ray data collection and crystallographic information pertaining to  $[\text{F}_5\text{Xe}(\text{FKrF})\text{AsF}_6]$  (**1**),  $[\text{F}_5\text{Xe}(\text{FKrF})_2\text{AsF}_6]$  (**2**),  $[\text{F}_5\text{Xe}(\text{FH})\text{AsF}_6]$  (**3**), and  $[\text{F}_5\text{Xe}(\text{FH})\text{SbF}_6]$  (**4**) are summarized in Table 1.

**Table 1:** Summary of X-ray crystal data and refinement results for  $[\text{F}_5\text{Xe}(\text{FKrF})\text{AsF}_6]$  (**1**),  $[\text{F}_5\text{Xe}(\text{FKrF})_2\text{AsF}_6]$  (**2**),  $[\text{F}_5\text{Xe}(\text{FH})\text{AsF}_6]$  (**3**), and  $[\text{F}_5\text{Xe}(\text{FH})\text{SbF}_6]$  (**4**).

Compound	1	2	3	4
Space group	$P2_1/n$	$P2_1/c$	$P2/c$	$P2_1/c$
<i>a</i> [Å]	9.03170(10)	9.3142(5)	12.2989(4)	6.3279(2)
<i>b</i> [Å]	9.7065(2)	8.0482(4)	6.4853(2)	15.2663(4)
<i>c</i> [Å]	12.1261(2)	16.1545(8)	10.6717(3)	8.8234(2)
$\beta$ [°]	106.8920(10)	95.942(3)	106.317(2)	92.6730(10)
<i>V</i> [Å <sup>3</sup> ]	1017.18(3)	1204.48(11)	816.91(4)	851.45(4)
<i>Z</i>	4	4	4	4
<i>M<sub>w</sub></i> [g mol <sup>-1</sup> ]	537.02	658.82	435.23	482.06
<i>D<sub>calcd</sub></i> [g cm <sup>-3</sup> ]	3.507	3.633	3.539	3.761
<i>T</i> [°C]	-173	-173	-173	-173
$\mu$ [mm <sup>-1</sup> ]	11.101	13.062	8.411	7.319
<i>R</i> <sub>1</sub> <sup>[a]</sup>	0.0288	0.0306	0.0228	0.0195
$wR$ <sub>2</sub> <sup>[b]</sup>	0.0561	0.0568	0.0452	0.0415

$$[a] R_1 = \sum |F_o| - |F_c| / \sum |F_o|. [b] wR_2 = [\sum (\omega(F_o^2 - F_c^2)^2) / \sum (\omega(F_o^2)^2)]^{1/2}.$$

**$[\text{F}_5\text{Xe}(\text{FKrF})\text{AsF}_6]$  (**1**) and  $[\text{F}_5\text{Xe}(\text{FKrF})_2\text{AsF}_6]$  (**2**).** The  $[\text{XeF}_5]^+$  cations are coordinated to four F atoms to give xenon coordination numbers, CN<sub>Xe</sub> = 5 + 4: one secondary bond from a  $\text{KrF}_2$  ligand and three from three  $[\text{AsF}_6]^-$  anions in  $[\text{F}_5\text{Xe}(\text{FKrF})\text{AsF}_6]$  (**1**) (Figure 1a; Supporting Information, Figures S1 and S2), whereas in the case of  $[\text{F}_5\text{Xe}(\text{FKrF})_2\text{AsF}_6]$  (**2**), two secondary bonds are from two  $\text{KrF}_2$  ligands and two are from two  $[\text{AsF}_6]^-$  anions (Figure 1b; Figures S3 and S4). The coordination spheres of the  $[\text{XeF}_5]^+$  cations in **1** and **2** are similar to their known xenon analogues,  $[\text{F}_5\text{Xe}(\text{FXeF})\text{AsF}_6]$ ,<sup>[19]</sup> and  $[\text{F}_5\text{Xe}(\text{FXeF})_2\text{AsF}_6]$ .<sup>[19]</sup> In the latter cases, the longer Xe--F<sub>As</sub> secondary bonds (1:1, 2.59, 3.03, and 3.15 Å; 1:2, 2.95 and 3.57 Å) are shorter than or equal to the sum of the Xe and F van der Waals radii (3.63,<sup>[23]</sup> 3.52<sup>[24]</sup> Å). Although the crystal structure of  $[\text{F}_5\text{Xe}(\text{FKrF})\text{AsF}_6]$  is isotopic with its xenon analogue,  $[\text{F}_5\text{Xe}(\text{FKrF})_2\text{AsF}_6]$  is not.

The trajectories of the four Xe--F secondary bonds in **1** and **2** avoid the Xe--F<sub>eq</sub> bond pair and valence electron lone pair (VELP) domains of the square-pyramidal  $[\text{XeF}_5]^+$  cation, where the lone pair lies on the pseudo C<sub>4</sub>-axis and is trans to the F<sub>ax</sub> atom of  $[\text{XeF}_5]^+$ . The  $[\text{AsF}_6]^-$  anions of **1** are mer-coordinated to three different  $[\text{XeF}_5]^+$  cations by means of asymmetric secondary Xe--F<sub>As</sub> bonds, where the *cis*-Xe--F<sub>As</sub> bond is notably shorter (2.5944(10) Å) than the *trans*-Xe--F<sub>As</sub> bonds (2.9147(10), 3.0572(11) Å). The three Xe--F<sub>As</sub> secondary bonds result in the layered structure depicted in Figure S1b. The  $[\text{AsF}_6]^-$  anions of **2** are asymmetrically *trans*-coordinated to two  $[\text{XeF}_5]^+$  cations (Xe--F<sub>As</sub>, 2.812(2), 3.124(2) Å), which form chains that run parallel to the *b*-axis of the unit cell (Figures S3b and S4). The  $\text{KrF}_2$  ligands coordinate to  $[\text{XeF}_5]^+$  by means of secondary Xe--F<sub>b</sub> bonds that are shorter ((**1**) 2.5139(9) Å; (**2**) 2.550(2), 2.576(2) Å) than the secondary Xe--F<sub>As</sub> bonds of the coordinated  $[\text{AsF}_6]^-$  anions (Table 2; Supporting Information, Tables S1 and S2). The Kr--F<sub>i</sub> and Kr--F<sub>b</sub> bond asymmetry is somewhat more pronounced in **1** (1.8393(12), 1.9367(9) Å) than in **2** (1.845(2), 1.927(2) Å and 1.851(2), 1.917(2) Å), which is attributed to stronger and shorter Xe--F<sub>b</sub> interactions in **1** than in **2**. Similar Kr--F<sub>i</sub> and Kr--F<sub>b</sub> bond length asymmetries

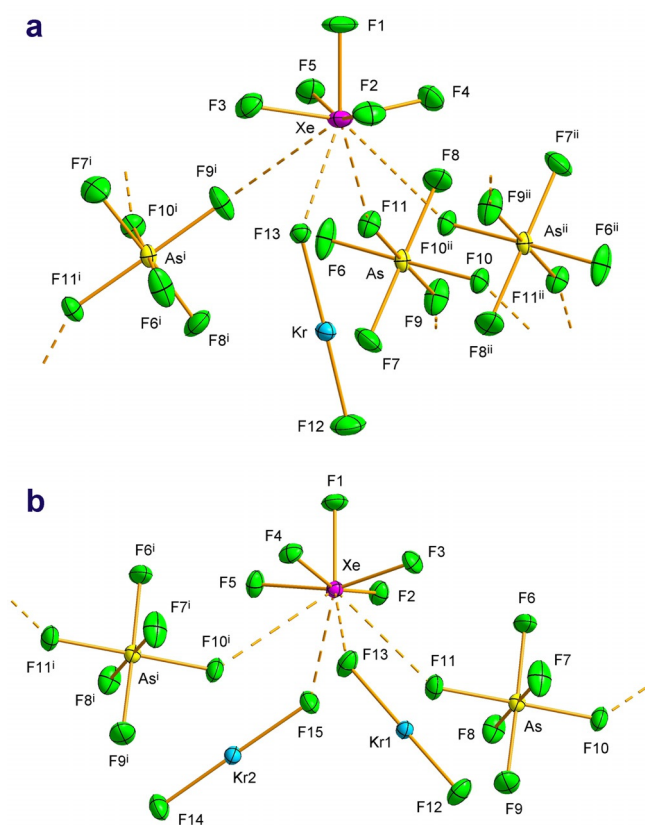


**Figure 1.** The X-ray crystal structure of a)  $[F_5Xe(FKrF)AsF_6]$  (**1**) and b)  $[F_3Xe(FKrF)_2AsF_6]$  (**2**) where the coordination environments of the Xe atom are expanded to include symmetry-generated atoms (symmetry codes: (1) (i)  $\frac{1}{2}-x, y-\frac{1}{2}, \frac{1}{2}-z$ ; (ii)  $1-x, 1-y, 1-z$ ; (2) (i)  $x, y+1, z$ ). Thermal ellipsoids are drawn at the 50% probability level.

**Table 2:** Selected experimental bond lengths for  $[F_5Xe(FKrF)AsF_6]$  (**1**) and  $[F_3Xe(FKrF)_2AsF_6]$  (**2**); and calculated<sup>[a]</sup> bond lengths and Wiberg bond indices (WBI) for  $[F_5Xe(FKrF)(AsF_6)_3]^{2-}$  (**1'**) and  $[F_3Xe(FKrF)_2(AsF_6)_2]^{2-}$  (**2'**).

	<b>1</b>	<b>1'</b>	<b>1'</b>	<b>2</b>	<b>2'</b>	<b>2'</b>
	Bond lengths [Å]		WBI	Bond lengths [Å]		WBI
Xe–F <sub>ax</sub>	1.8067(11)	1.919	0.550	1.813(2)	1.911	0.566
Xe–F <sub>eq</sub>	1.8394(12)	1.910	0.596	1.8371(14)	1.912	0.595
	1.8404(12)	1.910	0.595	1.8418(14)	1.903	0.607
	1.8455(13)	1.909	0.601	1.8449(14)	1.909	0.598
	1.8462(12)	1.910	0.600	1.8482(14)	1.925	0.597
Xe···F <sub>b</sub>	2.5139(9)	2.500	0.102	2.550(2)	2.784	0.037
				2.576(2)	2.626	0.069
Xe···F <sub>As</sub>	2.5944(10)	2.468	0.098	2.812(2)	2.480	0.096
	2.9147(10)	2.802	0.031	3.124(2)	2.563	0.068
	3.0572(11)	2.828	0.028			
Kr–F <sub>t</sub>	1.8393(12)	1.860	0.610	1.845(2)	1.862	0.603
				1.851(2)	1.874	0.576
Kr–F <sub>b</sub>	1.9367(9)	1.939	0.450	1.917(2)	1.909	0.502
				1.927(2)	1.930	0.464

[a] APFD/aVDZ(-PP)(Kr, Xe, As)/aVDZ(F).

are observed in the crystal structures of  $[FO_2Br(FKrF)_2AsF_6]$  (1.840(5) and 1.847(4) Å, 1.943(4) and 1.933(4) Å),<sup>[8]</sup>  $[Mg(FKrF)_4(AsF_6)_2]$  (1.817(2)–1.821(2) Å, 1.965(1)–1.979(1) Å),<sup>[10]</sup>  $[Hg(FKrF)_8]^{2+}$  (1.822(1)–1.852(1) Å, 1.933(1)–1.957(1) Å),<sup>[11]</sup> and  $KrF_2 \cdot CrOF_4$  (1.8489(9) and 1.9279(9) Å).<sup>[12]</sup> Regardless of their Kr–F bond asymmetries, the average Kr–F<sub>ub</sub> bond lengths ((**1**) 1.888(2) Å; (**2**) 1.886(2) and 1.884(2) Å) are comparable to the Kr–F bond lengths of  $\alpha$ - $KrF_2$  (1.894(5) Å)<sup>[15]</sup> and symmetrically bridged  $KrF_2$  in  $KrF_2 \cdot 2CrOF_4$  (1.8881(6) Å).<sup>[12]</sup> The F–Kr–F bond angles are essentially linear ((**1**) 178.49(6)°; (**2**) 178.47(8) and 179.40(7)°), whereas the Kr–F<sub>b</sub>···Xe angles are bent ((**1**) 133.24(5)°; (**2**) 137.40(8) and 141.80(7)°), as observed in all other  $KrF_2$  adducts.<sup>[8–12]</sup> The Kr–F<sub>b</sub>···Xe angles of **1** and **2** are similar to the Kr–F<sub>b</sub>···Br angles of  $[FO_2Br(FKrF)_2AsF_6]$  (132.1(2) and 139.9(2)°)<sup>[8]</sup> and are intermediate with respect to the range of Kr–F<sub>b</sub>···Mg angles observed for  $[Mg(FKrF)_4(AsF_6)_2]$  (121.84(7)–144.43(8)°).<sup>[10]</sup>

**[F<sub>5</sub>Xe(FH)AsF<sub>6</sub>] (3).** The asymmetric unit in the crystal structure of **3** is comprised of two  $[XeF_5]^+$  cations located on special positions, and an  $[AsF_6]^-$  anion and an HF molecule located on general positions (Figure 2; Figures S5 and S6). The Xe<sup>VI</sup> atoms have CN<sub>Xe</sub> = 5 + 4, where one  $[XeF_5]^+$  cation has four Xe···F<sub>As</sub> secondary bonds originating from the coordination of two pairs of symmetry-related  $[AsF_6]^-$  anions (2.647(2), 3.058(2) Å) whereas the other  $[XeF_5]^+$  cation interacts with two symmetry-related  $[AsF_6]^-$  anions through two secondary Xe···F<sub>As</sub> bonds (2.930(2) Å) and with two symmetry-related HF ligands through two short secondary Xe···F<sub>H</sub> bonds (2.656(2) Å) (Table S3). Each HF molecule is also H-bonded to two neighboring  $[AsF_6]^-$  anions with F<sub>H</sub>···F<sub>As</sub> distances of 2.545(2) Å, where the As–F bond of the H-bonded F ligand (1.746(2) Å) is the second longest As–F bond of the  $[AsF_6]^-$  anion. Each  $[AsF_6]^-$  anion also coordinates to three  $[XeF_5]^+$  cations in a *mer*-arrangement where the As–F bonds of the interacting fluorine atoms are slightly elongated (1.719(2), 1.727(2), 1.749(2) Å) with respect to the two non-interacting axial As–F bonds (1.701(2), 1.705(2) Å). The secondary Xe···F<sub>As</sub> and Xe···F<sub>H</sub> bonds

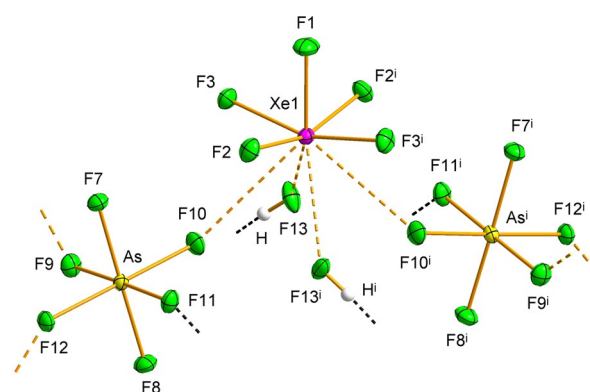


**Figure 2.** The crystal structure of  $[F_5Xe(FH)AsF_6]$  (**3**). The coordination environment of Xe1 is expanded to include symmetry-generated atoms (symmetry codes: (i)  $-x, y, \frac{1}{2}-z$ ). Thermal ellipsoids are drawn at the 50% probability level; hydrogen atoms are shown as spheres of arbitrary radius. The coordination environment of Xe2 is shown in Figure S5a.

result in corrugated layers that are parallel to the *ac*-plane and are stacked along the *b*-axis of the unit cell.

The Xe $\cdots$ F<sub>H</sub> secondary bonds of [F<sub>5</sub>Xe(FH)PnF<sub>6</sub>] (As, 2.656(2) Å; Sb, 2.6501(10) Å) are similar, but are significantly greater than those of [F<sub>3</sub>Xe(FH)Sb<sub>2</sub>F<sub>11</sub>] (2.462(2) Å)<sup>[25]</sup> and [FXe(FH)Sb<sub>2</sub>F<sub>11</sub>] (2.359(4) Å),<sup>[26]</sup> in accordance with the lower Lewis acidity of [XeF<sub>5</sub>]<sup>+</sup> relative to [XeF<sub>3</sub>]<sup>+</sup> and [XeF]<sup>+</sup>.<sup>[10,13,19]</sup>

A brief description of the crystal structure of the non-isotypic antimony analogue (**4**) is provided in the Supporting Information along with associated X-ray data (Figures S7 and S8, Table S3). The LT Raman spectrum of [F<sub>5</sub>Xe(FH)AsF<sub>6</sub>] (**3**) was also acquired (Figure S9, Table S4).

### Raman Spectroscopy

The LT solid-state Raman spectra of [F<sub>5</sub>Xe(FKrF)AsF<sub>6</sub>] (**1**) and [F<sub>5</sub>Xe(FKrF)<sub>2</sub>AsF<sub>6</sub>] (**2**) are depicted in Figure 3. Vibrational assignments for **1** were initially made by comparison with the calculated frequencies and assignments of gas-phase [F<sub>5</sub>Xe(FKrF)AsF<sub>6</sub>] (**1'**) (Table S5). Although this model accounts for the majority of experimental frequencies and intensities, several differences occur for modes that

mainly involve [AsF<sub>6</sub>]<sup>-</sup> anion displacements. This is expected because the coordination sphere of [XeF<sub>5</sub>]<sup>+</sup> in the gas-phase [F<sub>5</sub>Xe(FKrF)AsF<sub>6</sub>] model (**1'**, CN<sub>Xe</sub> = 5 + 3; Figure S10) differs from that of the solid-state structure **1** (CN<sub>Xe</sub> = 5 + 4). An alternative gas-phase model, [F<sub>5</sub>Xe(FKrF)(AsF<sub>6</sub>)<sub>3</sub>]<sup>2-</sup> (**1'**, CN<sub>Xe</sub> = 5 + 4, Figure 4a), addresses these differences and better reproduces the xenon coordination environment of [XeF<sub>5</sub>]<sup>+</sup> by coordination of two additional [AsF<sub>6</sub>]<sup>-</sup> anions to the [XeF<sub>5</sub>]<sup>+</sup> cation. The gas-phase [F<sub>5</sub>Xe(FKrF)<sub>2</sub>(AsF<sub>6</sub>)<sub>2</sub>]<sup>-</sup> model (**2'**, Figure 4b), which well reproduces the coordination environment of the [XeF<sub>5</sub>]<sup>+</sup> cation in **2**, was used to aid in the assignment of the Raman spectrum of **2**. The vibrational assignments of [XeF<sub>5</sub>]<sup>+</sup> and [AsF<sub>6</sub>]<sup>-</sup> in **1** and **2** were also aided by comparisons with those of [XeF<sub>5</sub>][AsF<sub>6</sub>],<sup>[27]</sup> [XeF<sub>5</sub>][BF<sub>4</sub>],<sup>[28]</sup> [XeF<sub>5</sub>][*fac*-OsO<sub>3</sub>F<sub>3</sub>],<sup>[29]</sup> [XeF<sub>5</sub>][*μ*-F(OsO<sub>3</sub>F<sub>2</sub>)<sub>2</sub>],<sup>[29]</sup> [XeF<sub>5</sub>]<sub>2</sub>[Cr<sub>2</sub>O<sub>2</sub>F<sub>8</sub>],<sup>[30]</sup> [XeF<sub>5</sub>][Xe<sub>2</sub>F<sub>11</sub>][CrOF<sub>5</sub>]<sub>2</sub>·2CrOF<sub>4</sub>,<sup>[30]</sup> [XeF<sub>5</sub>][M<sub>2</sub>O<sub>2</sub>F<sub>9</sub>] (M = Mo, W),<sup>[17]</sup> [F<sub>2</sub>OBr(FKrF)<sub>2</sub>AsF<sub>6</sub>],<sup>[8]</sup> and [Mg(FKrF)<sub>4</sub>(AsF<sub>6</sub>)<sub>2</sub>].<sup>[10]</sup> The experimental and calculated frequencies, their detailed assignments, and mode descriptions for **1** and **2** are provided in Tables S5 and S6, respectively. The vibrational frequencies and intensities of the gas-phase KrF<sub>2</sub> molecule were also calculated (Table S7) in order to estimate the degree to which the calculated frequencies of coordinated KrF<sub>2</sub> are over- or underestimated in **1'**, **1''**, and **2'**. The experimental vibrational frequencies and their trends are well reproduced by the calculated frequencies, with the exception of their ν(Kr–F) stretching frequencies, which are overestimated.

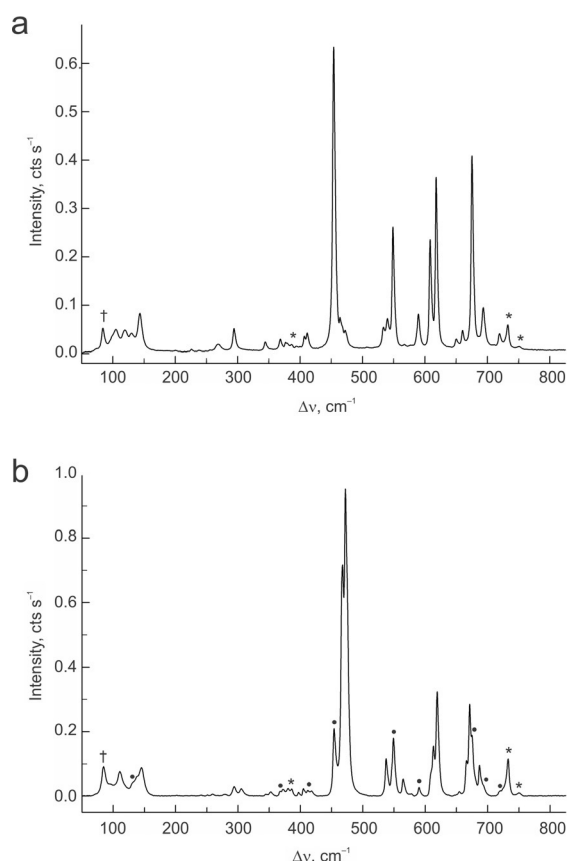


**Figure 3.** The Raman spectra of a) [F<sub>5</sub>Xe(FKrF)AsF<sub>6</sub>] (**1**) and b) [F<sub>5</sub>Xe(FKrF)<sub>2</sub>AsF<sub>6</sub>] (**2**) recorded at –144 and –161 °C, respectively, using 1064-nm excitation. The spectrum of (**2**) also shows bands due to (**1**), which are indicated by bullets (•) (Table S6, footnote c). Symbols (†) denote FEP sample tube bands (\*) and an instrumental artifact (†).

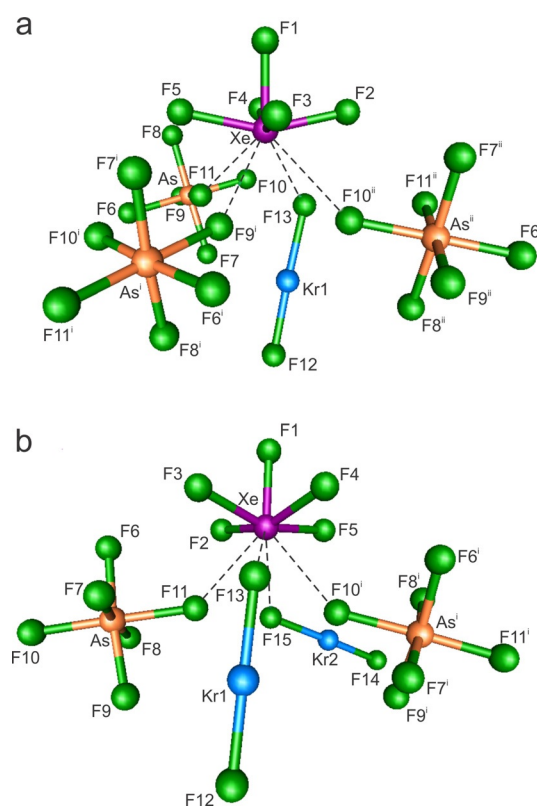


**Figure 4.** Calculated geometries [APFD/aVDZ(-PP)(Kr, Xe, As)/aVDZ(-F)] for a) [F<sub>5</sub>Xe(FKrF)(AsF<sub>6</sub>)<sub>3</sub>]<sup>2-</sup> (**1'**) and b) [F<sub>5</sub>Xe(FKrF)<sub>2</sub>(AsF<sub>6</sub>)<sub>2</sub>]<sup>-</sup> (**2'**).

**[F<sub>5</sub>Xe(FKrF)AsF<sub>6</sub>] (I).** Loss of the center of symmetry upon coordination of a fluorine atom of KrF<sub>2</sub> to Xe of [XeF<sub>5</sub>]<sup>+</sup> results in the appearance of two distinct stretching bands in the Raman spectrum that are assigned to  $\nu(\text{Kr}-\text{F}_b)$  and  $\nu(\text{Kr}-\text{F}_t)$ . The calculated vibrational displacements of **1**, show no significant intraligand coupling between the Kr–F<sub>b</sub> and Kr–F<sub>t</sub> stretching modes of coordinated KrF<sub>2</sub> ligands (Table S5). This contrasts with the KrF<sub>2</sub> ligands of KrF<sub>2</sub>·CrOF<sub>4</sub>,<sup>[12]</sup> which exhibit intraligand coupling between the  $\nu(\text{Kr}-\text{F}_b)$  and  $\nu(\text{Kr}-\text{F}_t)$  modes.

The most intense band in the Raman spectrum of **1** at 454 cm<sup>-1</sup> (calcd, 491 cm<sup>-1</sup>) is assigned to the  $\nu(\text{Kr}-\text{F}_b)$  stretching mode. As predicted, the  $\nu(\text{Kr}-\text{F}_t)$  stretching band corresponding to the shorter Kr–F<sub>t</sub> bond occurs at higher frequency, 533 cm<sup>-1</sup> (calcd, 585 cm<sup>-1</sup>). The experimental frequencies of  $\nu(\text{Kr}-\text{F}_b)$  and  $\nu(\text{Kr}-\text{F}_t)$  bracket that of free KrF<sub>2</sub> (464 cm<sup>-1</sup>), and are comparable to those of [F<sub>2</sub>OBr(FKrF)<sub>2</sub>AsF<sub>6</sub>] (443/472 and 533/549 cm<sup>-1</sup>).<sup>[8]</sup> The observed frequencies are in accordance with the experimental Kr–F bond length trend (Tables 2 and S1), with a similar trend observed for [F<sub>5</sub>Xe(FXeF)AsF<sub>6</sub>] (433 and 559 cm<sup>-1</sup>).<sup>[19]</sup>

The degeneracy of the  $\nu_2(\Pi_u)$  bending mode of free KrF<sub>2</sub> is removed upon coordination, which results in Raman-active  $\delta(\text{F}_t\text{KrF}_b)_{\text{i.p.}}$  and  $\delta(\text{F}_t\text{KrF}_b)_{\text{o.o.p.}}$  modes that bend in-plane and out-of-plane with respect to the XeF<sub>b</sub>KrF<sub>t</sub>-plane. The calculated out-of-plane bend couples with the two  $\rho_w(\text{F}_{\text{eq}}\text{XeF}_{\text{eq}})$  wagging modes of [XeF<sub>5</sub>]<sup>+</sup>, whereas the in-plane bend is not coupled. Both bands are predicted to have low relative Raman intensities and were observed as weak bands at 294 and 255 cm<sup>-1</sup> (calcd, 289 and 264 cm<sup>-1</sup>), respectively. Both bands are shifted to higher frequency relative to  $\nu_2(\Pi_u)$  of free KrF<sub>2</sub> (232.6 cm<sup>-1</sup>),<sup>[31]</sup> but have frequencies that are comparable to the corresponding modes of [F<sub>2</sub>OBr(FKrF)<sub>2</sub>AsF<sub>6</sub>] (301 and 254/266 cm<sup>-1</sup>).<sup>[8]</sup> The bands assigned to the  $\rho_t(\text{F}_t\text{KrF}_b)$  rocking and  $\rho_i(\text{F}_t\text{KrF}_b)$  torsional modes are predicted at 152 and 136 cm<sup>-1</sup> and were observed at 143 and 130 cm<sup>-1</sup>, respectively. Interestingly, and similar to the  $\delta(\text{F}_t\text{KrF}_b)$  bending modes, the out-of-plane torsional mode,  $\rho_i(\text{F}_t\text{KrF}_b)$ , also couples with the  $\rho_w(\text{F}_{\text{eq}}\text{XeF}_{\text{eq}})$  wagging modes of the cation, whereas the in-plane rocking mode,  $\rho_t(\text{F}_t\text{KrF}_b)$ , does not couple. The  $\delta(\text{XeF}_b\text{Kr})$  and  $\delta(\text{XeF}_{bA}\text{As})$  bends are predicted at very low frequencies, 60 and 71/74 cm<sup>-1</sup>, respectively, but could not be observed.

**[F<sub>5</sub>Xe(FKrF)<sub>2</sub>AsF<sub>6</sub>] (I').** Coordination of a second KrF<sub>2</sub> ligand to [XeF<sub>5</sub>]<sup>+</sup> results in additional splitting on the Kr–F stretching bands of the KrF<sub>2</sub> ligands that are due to intra- and interligand couplings. The bands at 543 and 564/567 cm<sup>-1</sup> (calcd, 585, 598 cm<sup>-1</sup>) are respectively assigned to modes that are predominantly coupled  $\nu(\text{Kr}-\text{F}_t)$  stretching modes,  $\{[\nu(\text{Kr}_1-\text{F}_{12}) - \nu(\text{Kr}_2-\text{F}_{14})] - [\nu(\text{Kr}_1-\text{F}_{13}) - \nu(\text{Kr}_2-\text{F}_{15})]_{\text{small}}\}$  and  $\{[\nu(\text{Kr}_1-\text{F}_{12}) + \nu(\text{Kr}_2-\text{F}_{14})] - [\nu(\text{Kr}_1-\text{F}_{13}) + \nu(\text{Kr}_2-\text{F}_{15})]_{\text{small}}\}$  (Table S6). Similar couplings, which are exclusively interligand couplings, also occur in other KrF<sub>2</sub> adducts that contain more than one NgF<sub>2</sub> ligand.<sup>[8–11]</sup> The bands at 466 and 472/474 cm<sup>-1</sup> (calcd, 507, 517 cm<sup>-1</sup>) are assigned to modes that are predominantly coupled  $\nu(\text{Kr}-\text{F}_b)$  stretching modes,  $[\nu(\text{Kr}_1-\text{F}_{13}) + \nu(\text{Kr}_1-\text{F}_{12})_{\text{small}}]$  and  $[\nu(\text{Kr}_2-\text{F}_{15}) + \nu(\text{Kr}_2-\text{F}_{14})_{\text{small}}]$ , respectively. Interestingly, and unlike adducts which contain more than one NgF<sub>2</sub> ligand,

there are no interligand couplings among the  $\nu(\text{Kr}-\text{F}_b)$  stretching modes. The room-temperature Raman spectrum of the xenon analogue, [F<sub>5</sub>Xe(FXeF)<sub>2</sub>AsF<sub>6</sub>], also displays split  $\nu(\text{Xe}-\text{F}_b)$  (420/438, 479 cm<sup>-1</sup>) and  $\nu(\text{Xe}-\text{F}_t)$  (542, 550 cm<sup>-1</sup>) bands which are likely due to vibrational mode coupling.<sup>[19]</sup>

Vibrational coupling between the KrF<sub>2</sub> ligands results in two out-of-plane,  $\delta(\text{F}_t\text{KrF}_b)_{\text{o.o.p.}}$  (calcd, 246, 247 cm<sup>-1</sup>), and two in-plane,  $\delta(\text{F}_t\text{KrF}_b)_{\text{i.p.}}$  (calcd, 275, 280 cm<sup>-1</sup>), bends which occur at 251 (o.o.p.) and 273/278 (i.p.) cm<sup>-1</sup>. The bands at 145 and 110 cm<sup>-1</sup>, are assigned to the in-plane  $\rho_t(\text{F}_t\text{KrF}_b)$  rocking mode (calcd, 136 cm<sup>-1</sup>) and the out-of-plane  $\rho_i(\text{F}_t\text{KrF}_b)$  torsional mode (calcd, 119 cm<sup>-1</sup>), respectively.

## Computational Results

The gas-phase geometries of [F<sub>5</sub>Xe(FKrF)AsF<sub>6</sub>] (**1''**) (Figure S10), the hypothetical model anions, [F<sub>5</sub>Xe(FKrF)(AsF<sub>6</sub>)<sub>3</sub>]<sup>2-</sup> (**1'**) and [F<sub>5</sub>Xe(FKrF)<sub>2</sub>(AsF<sub>6</sub>)<sub>2</sub>]<sup>-</sup> (**2'**) (Figure 4; Figure S11), KrF<sub>2</sub>, [XeF<sub>5</sub>]<sup>+</sup>, and IF<sub>5</sub> were optimized with all frequencies real at the APFD/aVDZ(-PP)(Xe, As, Kr)/aVDZ(F) level of theory (Tables S1, S2, S5–S8). The crystallographic coordinates were used as the starting geometries for the geometry optimizations. A limitation of the gas-phase structural models used for **1'** and **2'** is the isolated nature of the ion-pairs, which contrast with the extended (layer and chain) structures observed in the crystal structures of **1** and **2**. However, both models reproduce the coordination environment of xenon and therefore proved useful for the assignment of the Raman spectra and provided insights into the secondary bonding interactions among [XeF<sub>5</sub>]<sup>+</sup> and coordinated KrF<sub>2</sub> and [AsF<sub>6</sub>]<sup>-</sup>.

## Calculated Geometries

**[F<sub>5</sub>Xe(FKrF)AsF<sub>6</sub>] (I'') and [F<sub>5</sub>Xe(FKrF)(AsF<sub>6</sub>)<sub>3</sub>]<sup>2-</sup> (1').** The [F<sub>5</sub>Xe(FKrF)AsF<sub>6</sub>] (**1''**) ion-pair was initially calculated, but resulted in twisting of the [AsF<sub>6</sub>]<sup>-</sup> anion such that it coordinated in a bidentate fashion through two *cis*-fluorine ligands to the Xe atom to give CN<sub>Xe</sub> = 5 + 3 (Figure S10). In contrast, the [F<sub>5</sub>Xe(FKrF)(AsF<sub>6</sub>)<sub>3</sub>]<sup>2-</sup> model (**1'**) reproduced the experimental Xe coordination sphere (CN<sub>Xe</sub> = 5 + 4) and better reproduced the Xe---F<sub>b</sub> interactions and their avoidance of the Xe VELD and Xe–F<sub>eq</sub> bond pair domains.

The calculated Kr–F<sub>t</sub> bond length (1.860 Å) is shorter than the Kr–F<sub>b</sub> bond length (1.939 Å), as observed in the crystal structure (1.8393(12) and 1.9367(9) Å), and the average calculated Kr–F bond length (1.900 Å) is very similar to the calculated (1.889 Å) and experimental (1.894(5) Å)<sup>[15]</sup> bond lengths of free KrF<sub>2</sub>. The calculated F<sub>t</sub>–Kr–F<sub>b</sub> bond angle (176.7°) is in good agreement with the experimental value (178.49(6)°), whereas the Kr–F<sub>b</sub>---Xe bond angle (121.2°) is significantly smaller than the experimental value (133.24(5)°). The difference between the calculated and experimental Kr–F<sub>b</sub>---Xe angles is likely due to crystal packing and the deformability of this angle ( $\delta(\text{XeF}_b\text{Kr})$ , 60 cm<sup>-1</sup>).

The calculated Xe---F<sub>b/As</sub> contact distances (2.500, 2.468, 2.802, and 2.828 Å) are underestimated relative to their experimental values (2.5139(9), 2.5944(10), 2.9147(10), and 3.0572(11) Å), but reproduce the alternation of their long and short Xe---F secondary bonds in **1**. The shorter calculated contact distances are accompanied by large F<sub>ax</sub>-Xe---F<sub>b/As</sub> contact angles (142.1 and 141.1°) whereas long contact distances are accompanied by smaller F<sub>ax</sub>-Xe---F<sub>b/As</sub> contact angles (128.9 and 128.5°), in very good agreement with the corresponding angles in **1** (143.54(6) and 146.48(6)°; 129.90(6) and 124.67(6)°).

**[F<sub>5</sub>Xe(FKrF)<sub>2</sub>(AsF<sub>6</sub>)<sub>2</sub>]<sup>-</sup> (**2'**)**. The calculated geometrical parameters of the KrF<sub>2</sub> ligands reproduce the experimental values and trends in **2**, i.e., the shorter Kr-F<sub>t</sub> bond (calcd, 1.862 Å; exptl, 1.845(2) Å) is accompanied by a longer Kr-F<sub>b</sub> bond (calcd, 1.930 Å; exptl, 1.927(2) Å) for one KrF<sub>2</sub> ligand, and a longer Kr-F<sub>t</sub> bond (calcd, 1.874 Å; exptl, 1.851(2) Å) is accompanied by a shorter Kr-F<sub>b</sub> bond (calcd, 1.909 Å; exptl, 1.917(2) Å) for the other KrF<sub>2</sub> ligand. The near-linear F<sub>t</sub>-Kr-F<sub>b</sub> angles (178.47(8) and 179.40(7)°) of **2** are also reproduced (177.60 and 176.98°), but the Xe---F<sub>b</sub>-Kr angles (137.40(8) and 141.80(7)°) are significantly underestimated (123.99 and 124.71°). The difference is likely attributable to the absence of a secondary Xe---F<sub>As</sub> bond in **2'** that is *trans* to the bridging As-F bond in **2**. This results in bridging As-F (1.7285(14) and 1.7433(14) Å) and Xe---F<sub>As</sub> (2.812(2) and 3.124(2) Å) bond lengths that are overestimated (1.834 and 1.847 Å) and underestimated (2.480 and 2.563 Å), respectively, and F<sub>ax</sub>-Xe---F<sub>As</sub> angles (126.57(6) and 132.26(6)°) that are overestimated (139.81 and 140.53°). The Xe---F<sub>b</sub> bond lengths (2.550(2) and 2.576(2) Å) are overestimated (2.784 and 2.626 Å) and the F<sub>ax</sub>-Xe---F<sub>b</sub> angles (139.59(7) and 140.35(7)°) are underestimated (128.26 and 130.55°). As observed in **2**, there are two groups of alternating short and long calculated Xe---F<sub>b/As</sub> secondary bonds whose domains avoid the Xe VELP and Xe-F<sub>eq</sub> bond pair domains.

### Natural Bond Orbital (NBO) Analyses

The NBO analyses for [F<sub>5</sub>Xe(FKrF)(AsF<sub>6</sub>)<sub>3</sub>]<sup>2-</sup> (**1'**) and [F<sub>5</sub>Xe(FKrF)<sub>2</sub>(AsF<sub>6</sub>)<sub>2</sub>]<sup>-</sup> (**2'**) (Table S9) show the total positive charges on the [XeF<sub>5</sub>]<sup>+</sup> cations of **1'** (0.776) and **2'** (0.771) are notably less than the net positive charge of the uncoordinated [XeF<sub>5</sub>]<sup>+</sup> cation, and are consistent with charge transfer from the KrF<sub>2</sub> ligand (**1'**, 0.092 and **2'**, 0.092) and [AsF<sub>6</sub>]<sup>-</sup> (**1'**, -2.871 and **2'**, -1.864). Charge transfer mainly affects the F<sub>ax</sub> atoms of **1'** (-0.490) and **2'** (-0.475), which are significantly more negative relative to F<sub>ax</sub> of free [XeF<sub>5</sub>]<sup>+</sup> (-0.384). In contrast the average NPA charges of the F<sub>eq</sub> atoms of **1'** (-0.483) and **2'** (-0.486) are much closer to the F<sub>eq</sub> charges of free [XeF<sub>5</sub>]<sup>+</sup> (-0.447). The F<sub>b</sub> and F<sub>t</sub> charges of KrF<sub>2</sub> in **1'** (-0.513, F<sub>b</sub> and -0.453, F<sub>t</sub>) and **2'** (-0.526, F<sub>b</sub> and -0.456, F<sub>t</sub>; -0.514, F<sub>b</sub> and -0.475, F<sub>t</sub>) bracket that of free KrF<sub>2</sub> (-0.492). The charge distribution is consistent with an axially distorted KrF<sub>2</sub> ligand in which partial removal of the bridging fluorine atom by the Lewis acidic [XeF<sub>5</sub>]<sup>+</sup> cation results in more KrF<sup>+</sup> character and correspondingly shorter Kr-F<sub>t</sub> and longer Kr-F<sub>b</sub> bonds (Tables S1 and S2). The Kr-F<sub>t</sub> and Kr-F<sub>b</sub> Wiberg bond

indices of **1'** (Kr-F<sub>t</sub>, 0.610 and Kr-F<sub>b</sub>, 0.450) and **2'** (Kr-F<sub>t</sub>, 0.603 and Kr-F<sub>b</sub>, 0.464; Kr-F<sub>t</sub>, 0.576 and Kr-F<sub>b</sub>, 0.502) bracket those of KrF<sub>2</sub> (0.551). The small Xe-F<sub>b</sub> bond indices of **1'** (0.102) and **2'** (0.069 and 0.037), and the low degree of charge transfer from KrF<sub>2</sub> to [XeF<sub>5</sub>]<sup>+</sup> are consistent with predominantly electrostatic secondary bonding interactions between the Xe and the F<sub>b</sub> atom(s) of the KrF<sub>2</sub> ligand(s) and the long experimental and calculated Xe---F<sub>b</sub> bonds observed in **1**, **2**, **1'**, and **2'** (Tables S1 and S2). The NBO analyses of [AsF<sub>6</sub>]<sup>-</sup> in **1'** and **2'** show that the larger Xe---F<sub>As</sub> bond indices of **1'** (0.098) and **2'** (0.096) correspond to smaller As-F bond indices of **1'** (0.386) and **2'** (0.382). This is in accordance with the shorter Xe---F<sub>As</sub> bonds (calcd, **1'**: 2.468 Å; **2'**: 2.480 Å; exptl, **1**: 2.5944(10) Å; **2**: 2.812(2) Å) and correspondingly longer As-F bridge bonds (calcd, **1'**: 1.844 Å; **2'**: 1.847 Å; exptl, **1**: 1.7559(10) Å; **2**: 1.7433(14) Å).

### Electron Localization Function (ELF) Analyses

The Electron Localization Function analyses<sup>[32,33]</sup> were carried out for [F<sub>5</sub>Xe(FKrF)(AsF<sub>6</sub>)<sub>3</sub>]<sup>2-</sup>, [F<sub>5</sub>Xe(FKrF)<sub>2</sub>(AsF<sub>6</sub>)<sub>2</sub>]<sup>-</sup>, KrF<sub>2</sub>, [XeF<sub>5</sub>]<sup>+</sup>, and isoelectronic IF<sub>5</sub>. The abbreviations in the ensuing discussion denote electron localization function ( $\eta(r)$ ); core basin (C(Ng), C(As)); monosynaptic valence basins (V(F) and V(Ng)); and *f*, a localization domain that is bounded by the isosurface,  $\eta(r) = f$ . The ELF isosurface plots for the aforementioned species at  $\eta(r) = 0.55$  are depicted in Figure 5 and Figure S12.

The ELF analyses of [F<sub>5</sub>Xe(FKrF)(AsF<sub>6</sub>)<sub>3</sub>]<sup>2-</sup>, [F<sub>5</sub>Xe(FKrF)<sub>2</sub>(AsF<sub>6</sub>)<sub>2</sub>]<sup>-</sup>, KrF<sub>2</sub>, [XeF<sub>5</sub>]<sup>+</sup>, and IF<sub>5</sub> display only monosynaptic Xe, Kr, As, F, and I valence basins in accordance with the polar-covalent characters of their bonds. The toroidal shapes of the Kr valence basins result from the combination of the three valence electron lone-pair (VELP) domains of Kr, with the atomic core electron basin (C(Kr)) lying at the center of the torus. The perturbations of the toroidal V(Kr) basin of [F<sub>5</sub>Xe(FKrF)(AsF<sub>6</sub>)<sub>3</sub>]<sup>2-</sup> and one of the toroidal V(Kr)

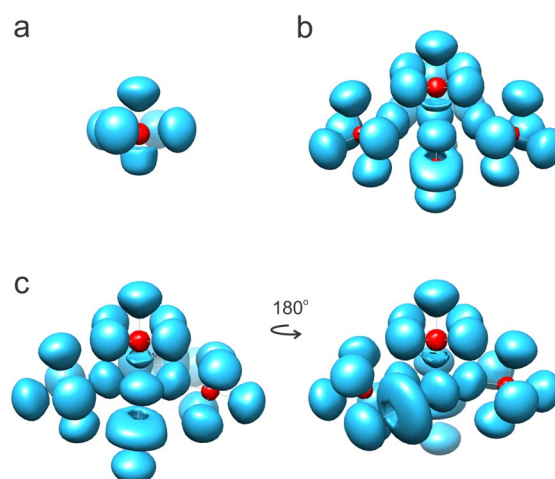


**Figure 5.** ELF isosurface plots [APFD/aVDZ(-PP)(Kr, Xe, As)/aVDZ(F)],  $\eta(r) = 0.55$ , for a) [XeF<sub>5</sub>]<sup>+</sup>, b) [F<sub>5</sub>Xe(FKrF)(AsF<sub>6</sub>)<sub>3</sub>]<sup>2-</sup>, and c) [F<sub>5</sub>Xe(FKrF)<sub>2</sub>(AsF<sub>6</sub>)<sub>2</sub>]<sup>-</sup>. Color code: core basin (red); C(Ng), C(As); monosynaptic valence basin (blue); V(F), V(Ng).

basins of  $[\text{F}_5\text{Xe}(\text{FKrF})_2(\text{AsF}_6)_2]^-$  arise from accommodation of the V(Kr) basins to their immediate environments (Figure 5). In both instances, the krypton valence basin torus of one  $\text{KrF}_2$  ligand is flattened parallel to the  $\text{KrF}_2$  molecular axis because the ligand is sandwiched between the fluorine valence basins of neighboring  $[\text{AsF}_6]^-$  ions (Figure 5). In contrast, the second  $\text{KrF}_2$  ligand of  $[\text{F}_5\text{Xe}(\text{FKrF})_2(\text{AsF}_6)_2]^-$  is less sterically congested which results in a V(Kr) basin that is essentially unperturbed, closely resembling the toroidal V(Kr) valence basin of free  $\text{KrF}_2$  (Figure S12). Small perturbations of the toroidal V(Ng) basins (Ng = Kr, Xe) of  $\text{NgF}_2 \cdot \text{CrOF}_4$  and  $\text{NgF}_2 \cdot 2\text{CrOF}_4$  have also been noted and attributed to the asymmetries of their immediate environments.<sup>[12]</sup>

The valence basins, V(Xe) and V(I) of Xe and I in the isoelectronic  $[\text{XeF}_5]^+$  cation and  $\text{IF}_5$ , correspond to stereoactive electron lone-pairs, where the  $[\text{XeF}_5]^+$  VELP ( $2.14 \text{ \AA}^3$ ) is significantly contracted relative to that of  $\text{IF}_5$  ( $3.08 \text{ \AA}^3$ ), in accordance with the higher charge on Xe (3.17) of  $[\text{XeF}_5]^+$  relative to that of I (2.90) in  $\text{IF}_5$  (also see MEPS analyses).

Notable differences occur between the Xe VELP distributions of the adduct-cations, where the VELP volumes and shapes accommodate to the spaces provided by the neighboring V(F) basins of the  $\text{KrF}_2$  ligands and  $[\text{AsF}_6]^-$  ions. The Xe VELPs of  $[\text{F}_5\text{Xe}(\text{FKrF})(\text{AsF}_6)_3]^{2-}$  and  $[\text{F}_5\text{Xe}(\text{FKrF})_2(\text{AsF}_6)_2]^-$  are sterically more congested in their nine-coordinate Xe environments, where the Xe VELPs are notably flattened and their volumes ( $0.44$  and  $0.46 \text{ \AA}^3$ , respectively) are significantly reduced with respect to those of  $[\text{XeF}_5]^+$  and  $\text{IF}_5$  (vide supra). Similar steric influences on the  $\text{Xe}^{\text{VI}}$  VELP volume have been noted for the series,  $\text{XeF}_6$  ( $C_{3v}$ ),  $\text{F}_6\text{XeNCCH}_3$ , and  $\text{F}_6\text{Xe}(\text{NCCH}_3)_2$ .<sup>[34]</sup>

### Molecular Electrostatic Potential Surface (MEPS) Analyses

The MEPS isosurfaces of  $[\text{XeF}_5]^+$  and isoelectronic  $\text{IF}_5$  are depicted in Figure 6. Their isosurfaces have regions of high EP (Xe,  $773 \text{ kJ mol}^{-1}$  and I,  $228 \text{ kJ mol}^{-1}$ ), which are located trans to their  $\text{F}_{\text{ax}}$  atoms. The xenon atom is significantly more electrophilic than the iodine atom, and the MEPS maxima of the fluorine ligand isosurfaces of  $[\text{XeF}_5]^+$  are significantly more positive than those of  $\text{IF}_5$  which have small negative values, in accordance with their NPA charges (Table S9).

Examination of the top 5% of the positive EP ranges in  $[\text{XeF}_5]^+$  and  $\text{IF}_5$  (Figure 6) allowed the visualization of four regions of higher EP on the xenon and iodine MEPS isosurfaces (Xe,  $798 \text{ kJ mol}^{-1}$  and I,  $236 \text{ kJ mol}^{-1}$ ) that are located at the intersections of the  $\text{F}_{\text{eq}}$  isosurfaces. Similar regions have been reported for  $\text{IF}_5$  and  $\text{XeF}_4$ .<sup>[35]</sup> These regions are symmetrically disposed with respect to the xenon and iodine VELPs, which are trans to  $\text{F}_{\text{ax}}$  atoms of  $[\text{XeF}_5]^+$  and  $\text{IF}_5$ . The experimental and calculated trajectories of the secondary Xe $\cdots$ F<sub>b</sub> and Xe $\cdots$ F<sub>As</sub> bonds in **1** (Figure S1), **2** (Figure S3), **1'** and **2'** (Figure S11) are staggered with respect to the  $\text{F}_{\text{eq}}$  atoms of  $[\text{XeF}_5]^+$  and avoid the xenon VELP, in accordance with the calculated positions of the four EP maxima on xenon. The crystal structure of  $\text{XeF}_2 \cdot \text{IF}_5$  exhibits similar features, i.e., four

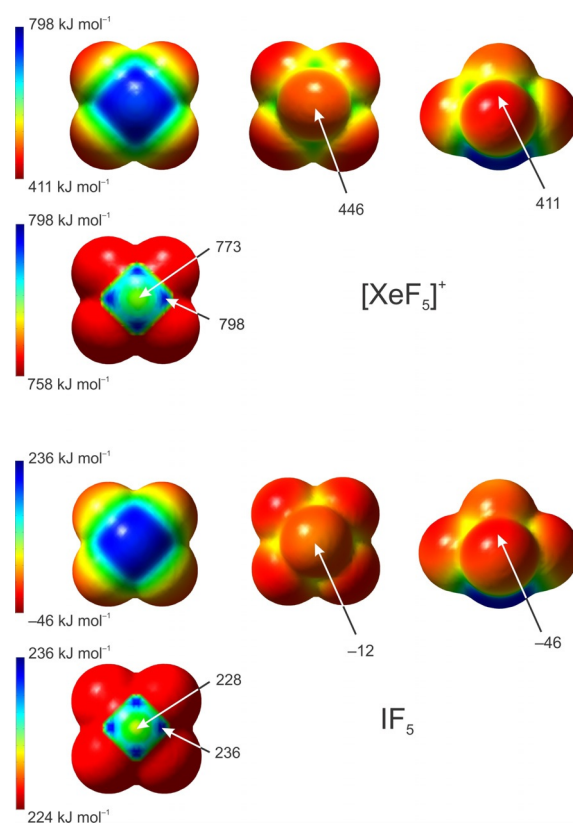


**Figure 6.** The molecular electrostatic potential surface (MEPS) contours calculated at the  $0.001 \text{ e-bohr}^{-3}$  isosurfaces of  $[\text{XeF}_5]^+$  and  $\text{IF}_5$  and the top 5% of the positive electrostatic potential range (bottom left). The extrema of selected electrostatic potentials are indicated by arrows. The optimized geometries and MEPS were calculated at the APFD/aVDZ-(PP)(Xe, I)/aVDZ(F) level of theory.

I $\cdots$ F<sub>b</sub> secondary bonds whose trajectories are staggered with respect to the I $\cdots$ F<sub>eq</sub> bond domains of  $\text{IF}_5$  and avoid the VELP domain of iodine.<sup>[36]</sup> The electrostatic nature of the secondary Xe $\cdots$ F<sub>b</sub> bonds is also supported by the Wiberg bond indices obtained for **1'** and **2'** (Table S9), and may be ascribed to  $\sigma$ -hole bonding. The MEPS of  $\text{XeO}_3$  ( $C_{3v}$ ) also show discrete regions of higher EP on the xenon MEPS isosurface, which were visualized by examination of the top 20% of the xenon MEPS isosurface.<sup>[37]</sup> In contrast with  $[\text{XeF}_5]^+$  and  $\text{IF}_5$ , three regions of higher EP of  $\text{XeO}_3$  are located trans to the highly electronegative oxygen atoms of the primary Xe $\cdots$ O bonds, a characteristic of  $\sigma$ -hole bonding,<sup>[38]</sup> and have contact trajectories that are staggered with respect to these bonds.

### Conclusion

The present study provides the first instances where both chemically bound krypton and xenon are present in the same compound. The  $[\text{F}_5\text{Xe}(\text{FKrF})\text{AsF}_6]$  and  $[\text{F}_5\text{Xe}(\text{FKrF})_2\text{AsF}_6]$  complexes have been isolated in macroscopic quantities and structurally characterized by X-ray crystallography and Raman spectroscopy. Their syntheses, which significantly extend the limited chemistry of krypton and the  $\text{XeF}_2$ - $\text{KrF}_2$  analogy, provide a new class of coordination complex in which

KrF<sub>2</sub> coordinates through a fluorine atom to Xe<sup>VI</sup> of the [XeF<sub>5</sub>]<sup>+</sup> cation. The stabilities of these complexes are reliant on the Lewis acidity of [XeF<sub>5</sub>]<sup>+</sup> and its resistance to oxidation by the potent oxidative fluorinator, KrF<sub>2</sub>. NBO, ELF, and MEPS analyses demonstrate that the bonding interactions between the fluorine bridge atom of KrF<sub>2</sub> and the Lewis acidic xenon atom are essentially noncovalent and may be ascribed to  $\sigma$ -hole bonding. The HF solvates, [F<sub>5</sub>Xe(FH)PnF<sub>6</sub>] (Pn = As, Sb), also characterized in this study, provide rare examples of HF coordinated to Xe<sup>VI</sup>.

## Experimental Section

**Cautionary statements** relating to the safe handling of XeF<sub>6</sub>, KrF<sub>2</sub>, and [XeF<sub>5</sub>]<sup>+</sup> salts are provided in the Supporting Information. Details relating to the apparatus, starting materials, syntheses, low-temperature crystal mounting, X-ray data collection and refinement, Raman spectroscopy, and computational details are provided in the Supporting Information. Details of the crystal structure investigations may be obtained from the joint CCDC/FIZ Karlsruhe online deposition service by quoting the deposition numbers CSD 2000547 (1), 2000548 (2), 2000549 (3), and 2000550 (4).

## Acknowledgements

Support from the Marie Curie International Outgoing Fellowship (M.L.) within the 7<sup>th</sup> European Community Framework Programme; the Natural Sciences and Engineering Research Council of Canada, in the form of a Discovery Grant (G.J.S.); and the Slovenian Research Agency, in the form of the Research Programme P1-0045 (M.L.), are gratefully acknowledged. We also thank SHARCNet (Shared Hierarchical Academic Research Computing Network; [www.sharcnet.ca](http://www.sharcnet.ca)) and Compute Canada ([www.computecanada.ca](http://www.computecanada.ca)) for providing computational resources. We are grateful to Mark R. Bortolus for improving the crystal structure solution of [F<sub>5</sub>Xe(FH)AsF<sub>6</sub>].

## Conflict of interest

The authors declare no conflict of interest.

**Keywords:** fluorine chemistry · hypervalent compounds · krypton and xenon compounds · Raman spectroscopy · X-ray crystallography

- [1] F. Schreiner, J. G. Malm, J. C. Hindman, *J. Am. Chem. Soc.* **1965**, *87*, 25–28, and references therein.
- [2] N. Bartlett, *Proc. Chem. Soc.* **1962**, 6, 218.
- [3] L. Graham, O. Graudejus, N. K. Jha, N. Bartlett, *Coord. Chem. Rev.* **2000**, *197*, 321–334.
- [4] R. Craciun, D. Picone, R. T. Long, S. Li, D. A. Dixon, K. A. Peterson, K. O. Christe, *Inorg. Chem.* **2010**, *49*, 1056–1070.
- [5] J. F. Lehmann, H. P. A. Mercier, G. J. Schrobilgen, *Coord. Chem. Rev.* **2002**, *233–234*, 1–39.
- [6] D. S. Brock, G. J. Schrobilgen, B. Žemva, In *Comprehensive Inorganic Chemistry II, Vol. 1* (Eds.: J. Reedijk, K. Poepplmeier), Elsevier, Oxford, **2013**, pp. 755–822.
- [7] M. Lozinšek, G. J. Schrobilgen, *Nat. Chem.* **2016**, *8*, 732.
- [8] D. S. Brock, J. J. Casalis de Pury, H. P. A. Mercier, G. J. Schrobilgen, B. Silvi, *J. Am. Chem. Soc.* **2010**, *132*, 3533–3542.
- [9] J. R. DeBackere, H. P. A. Mercier, G. J. Schrobilgen, *J. Am. Chem. Soc.* **2014**, *136*, 3888–3903.
- [10] M. Lozinšek, H. P. A. Mercier, D. S. Brock, B. Žemva, G. J. Schrobilgen, *Angew. Chem. Int. Ed.* **2017**, *56*, 6251–6254; *Angew. Chem.* **2017**, *129*, 6347–6350.
- [11] J. R. DeBackere, G. J. Schrobilgen, *Angew. Chem. Int. Ed.* **2018**, *57*, 13167–13171; *Angew. Chem.* **2018**, *130*, 13351–13355.
- [12] H. P. A. Mercier, U. Breddemann, D. S. Brock, M. R. Bortolus, G. J. Schrobilgen, *Chem. Eur. J.* **2019**, *25*, 12105–12119.
- [13] D. S. Brock, J. J. Casalis de Pury, H. P. A. Mercier, G. J. Schrobilgen, B. Silvi, *Inorg. Chem.* **2010**, *49*, 6673–6689.
- [14] M. Tramšek, P. Benkič, B. Žemva, *Inorg. Chem.* **2004**, *43*, 699–703.
- [15] J. F. Lehmann, D. A. Dixon, G. J. Schrobilgen, *Inorg. Chem.* **2001**, *40*, 3002–3017.
- [16] K. Radan, E. Goreschnik, B. Žemva, *Angew. Chem. Int. Ed.* **2014**, *53*, 13715–13719; *Angew. Chem.* **2014**, *126*, 13935–13939.
- [17] M. R. Bortolus, H. P. A. Mercier, G. J. Schrobilgen, *Chem. Eur. J.* **2020**, *26*, 8935–8950, and references therein.
- [18] N. Bartlett, M. Wechsberg, *Z. Anorg. Allg. Chem.* **1971**, *385*, 5–17.
- [19] B. Žemva, A. Jesih, D. H. Templeton, A. Zalkin, A. K. Cheetham, N. Bartlett, *J. Am. Chem. Soc.* **1987**, *109*, 7420–7427.
- [20] B. Žemva, L. Golič, J. Slivnik, *Vestn. Slov. Kem. Drus.* **1983**, *30*, 365–376.
- [21] B. E. Pointner, R. J. Suontamo, G. J. Schrobilgen, *Inorg. Chem.* **2006**, *45*, 1517–1534.
- [22] M. Tramšek, B. Žemva, *J. Fluorine Chem.* **2006**, *127*, 1275–1284.
- [23] A. Bondi, *J. Phys. Chem.* **1964**, *68*, 441–451.
- [24] S. Alvarez, *Dalton Trans.* **2013**, *42*, 8617–8636.
- [25] D. S. Brock, H. P. A. Mercier, G. J. Schrobilgen, *J. Am. Chem. Soc.* **2013**, *135*, 5089–5104.
- [26] T. Drews, K. Seppelt, *Angew. Chem. Int. Ed. Engl.* **1997**, *36*, 273–274; *Angew. Chem.* **1997**, *109*, 264–266.
- [27] K. O. Christe, E. C. Curtis, R. D. Wilson, *J. Inorg. Nucl. Chem. Supplement* **1976**, *28*, 159–165.
- [28] C. J. Adams, N. Bartlett, *Isr. J. Chem.* **1978**, *17*, 114–125.
- [29] M. J. Hughes, H. P. A. Mercier, G. J. Schrobilgen, *Inorg. Chem.* **2010**, *49*, 3501–3515.
- [30] J. T. Goettel, M. R. Bortolus, D. G. Stuart, H. P. A. Mercier, G. J. Schrobilgen, *Chem. Eur. J.* **2019**, *25*, 15815–15829.
- [31] H. H. Claassen, G. L. Goodman, J. G. Malm, F. Schreiner, *J. Chem. Phys.* **1965**, *42*, 1229–1232.
- [32] A. D. Becke, K. E. Edgecombe, *J. Chem. Phys.* **1990**, *92*, 5397–5403.
- [33] B. Silvi, A. Savin, *Nature* **1994**, *371*, 683–686.
- [34] J. Haner, K. Matsumoto, H. P. A. Mercier, G. J. Schrobilgen, *Chem. Eur. J.* **2016**, *22*, 4833–4842.
- [35] O. Kirshenboim, S. Kozuch, *J. Phys. Chem. A* **2016**, *120*, 9431–9445.
- [36] G. R. Jones, R. D. Burbank, N. Bartlett, *Inorg. Chem.* **1970**, *9*, 2264–2268.
- [37] K. M. Marczenko, H. P. A. Mercier, G. J. Schrobilgen, *Angew. Chem. Int. Ed.* **2018**, *57*, 12448–12452; *Angew. Chem.* **2018**, *130*, 12628–12632.
- [38] P. Politzer, J. S. Murray, T. Clark, G. Resnati, *Phys. Chem. Chem. Phys.* **2017**, *19*, 32166–32178.

Manuscript received: November 2, 2020

Accepted manuscript online: November 26, 2020

Version of record online: March 1, 2021